



Research Paper

New adaptive low-dissipation central-upwind schemes

Shaoshuai Chu ^{a,b}, Alexander Kurganov ^{c,*}, Igor Menshov ^d^a Department of Mathematics, RWTH Aachen University, 52056 Aachen, Germany^b Department of Mathematics and Shenzhen International Center for Mathematics, Southern University of Science and Technology, Shenzhen, 518055, China^c Department of Mathematics, Shenzhen International Center for Mathematics and Guangdong Provincial Key Laboratory of Computational Science and Material Design, Southern University of Science and Technology, Shenzhen, 518055, China^d Keldysh Institute for Applied Mathematics RAS, Moscow 125047, Russia

ARTICLE INFO

MSC:
 65M08
 76M12
 76L05
 35L65

Keywords:

Low-dissipation central-upwind schemes
 Smoothness indicator
 Overcompressive limiters
 Dissipative limiters
 Euler equations of gas dynamics

ABSTRACT

We introduce new second-order adaptive low-dissipation central-upwind (LDCU) schemes for the one- and two-dimensional hyperbolic systems of conservation laws. The new adaptive LDCU schemes employ the recently proposed LDCU numerical fluxes computed using the point values reconstructed with the help of adaptively selected nonlinear limiters. To this end, we use a smoothness indicator to detect “rough” parts of the computed solution, where the piecewise linear reconstruction is performed using an overcompressive limiter, which leads to extremely sharp resolution of shock and contact waves. In the “smooth” areas, we use a more dissipative limiter to prevent appearance of artificial kinks and staircase-like structures there. In order to avoid oscillations, we perform the reconstruction in the local characteristic variables obtained using the local characteristic decomposition. We use a smoothness indicator from Löhner (1987) [34] and apply the developed schemes to the one- and two-dimensional Euler equations of gas dynamics. The obtained numerical results clearly demonstrate that the new adaptive LDCU schemes outperform the original ones.

1. Introduction

This paper focuses on developing new adaptive numerical methods for the hyperbolic systems of conservation laws, which in the one- (1-D) and two-dimensional (2-D) cases, read as

$$\mathbf{U}_t + \mathbf{F}(\mathbf{U})_x = \mathbf{0}, \quad (1.1)$$

and

$$\mathbf{U}_t + \mathbf{F}(\mathbf{U})_x + \mathbf{G}(\mathbf{U})_y = \mathbf{0}, \quad (1.2)$$

respectively. Here, x and y are spatial variables, t is the time, $\mathbf{U} \in \mathbb{R}^d$ is a vector of unknown functions, and $\mathbf{F} : \mathbb{R}^d \rightarrow \mathbb{R}^d$ and $\mathbf{G} : \mathbb{R}^d \rightarrow \mathbb{R}^d$ are nonlinear fluxes.

* Corresponding author.

E-mail addresses: chuss2019@mail.sustech.edu.cn (S. Chu), alexander@sustech.edu.cn (A. Kurganov), menshov@kiam.ru (I. Menshov).

<https://doi.org/10.1016/j.apnum.2024.11.010>

Received 31 May 2024; Received in revised form 3 September 2024; Accepted 12 November 2024

It is well-known that even when the initial data are smooth, solutions of (1.1) and (1.2) can produce extremely complex nonsmooth wave patterns including shocks, rarefactions, and contact discontinuities. This makes it quite challenging to develop accurate and reliable shock-capturing numerical methods for (1.1) and (1.2).

A library of numerical methods for the studied systems has been introduced since the pioneering works of Friedrichs [11], Lax [30], and Godunov [16]. We refer the reader to the monographs and review papers [2,15,21,31,43,47] and references therein, where one can find a description of many existing numerical methods. In this paper, we restrict our consideration to semi-discrete finite-volume (FV) methods, where the solution, represented in terms of its cell averages, is evolved in time with the help of the numerical fluxes, computed, in turn, using the reconstructed point values of \mathbf{U} at the boundaries of the FV cells. Many of such schemes are upwind in the sense that their numerical fluxes are based on either exact or approximate solution of the (generalized) Riemann problems arising at each cell interface. We, however, focus on the Riemann-solver-free central-upwind (CU) schemes, which provide one with accurate, efficient, and robust tools for a wide variety of hyperbolic systems. The CU schemes belong to the class of non-oscillatory central schemes, but they have a certain upwind nature as they rely on the local one-sided speeds of propagation, which can be estimated using the largest and smallest eigenvalues of the corresponding Jacobians. The original CU schemes from [27,28] contain relatively large amount of numerical dissipation, which was reduced in [25] and recently in [4,29], where built-in “anti-diffusion” terms were introduced. The amount of numerical dissipation can be also reduced by applying the local characteristic decomposition (LCD) technique to the numerical diffusion of the CU fluxes; see [3].

In this paper, we use the low-dissipation CU (LDCU) numerical fluxes from [4], and further enhance the resolution of the “rough” parts of the computed solution by applying a new scheme adaption approach: The point values used to evaluate the LDCU fluxes are reconstructed with the help of adaptively selected nonlinear limiters, which are, in general, required to make the reconstructed point values non-oscillatory. A variety of limiters are available; see, e.g., [2,21,31,32,36,46,47] and references therein. Many of the limiters can be classified as dissipative, compressive, or overcompressive as it was done in [32]. The use of compressive and overcompressive limiters leads to very sharp resolution of discontinuous parts of the approximated solution, while dissipative limiters may smear the jumps. At the same time, applying compressive and overcompressive limiters in the smooth areas typically results in the artificial sharpening of the smooth solution profiles, that is, in the appearance of kinks or staircase-like structures, or even non-physical jump discontinuities.

We therefore switch between different limiters. To this end, we need to automatically detect “rough” (nonsmooth) parts of the computed solution with the help of a smoothness indicator (SI). Many different SIs are readily available; see, e.g., [1,5,8,12–14,19,20,23,24,26,34,37,39,45,48,50,53,54]. We have tested the SIs based on minmod shock indicators [20,45,53], entropy production [37], weak local residuals [5,23,24,26], radial based function [50], and neural network [54]. They all lead to descent adaptive schemes, but none of them was truly robust in the sense that we could not achieve extremely high resolution of constant waves without affecting a quality of resolution of smooth parts of the computed solution. The only SI, which robustly performed in all of the tested numerical examples was the SI proposed in [34] (also see [35]). In the areas identified as being “rough”, we use the overcompressive SBM limiters from [32], while switching to the dissipative Minmod2 limiter elsewhere. It is well-known that the use of any of these two limiters may lead to numerical oscillations in the vicinities of shock and contact discontinuities. In order to reduce these oscillations, we perform the reconstruction in the local characteristic variables rather than in the conservative or primitive ones (this strategy was advocated in, e.g., [38]). We switch to the characteristic variables using the LCD, which is often used in the context of high-order schemes, but can also be implemented to enhance the resolution of second-order schemes; see, e.g., [3,22,38,43] and references therein.

The paper is organized as follows. In §2, we review the recently proposed 1-D LDCU scheme from [4] and then introduce the new adaptive LDCU scheme. In §3, we extend the proposed adaptive scheme to the 2-D case. In §4, we apply the developed schemes to a number of 1-D and 2-D numerical examples for the Euler equations of gas dynamics. We demonstrate that the adaptive LDCU schemes contain substantially smaller amount of numerical dissipation and achieve much higher resolution compared with the LDCU schemes based on the Minmod2 limiters applied throughout the entire computational domain. Finally, we give some concluding remarks in §5.

2. One-dimensional scheme adaption algorithm

In this section, we consider the 1-D conservation laws (1.1) and describe the 1-D adaptive algorithm.

2.1. 1-D low-dissipation central-upwind (LDCU) schemes

Assume that the computational domain is covered with the uniform cells $C_j := [x_{j-\frac{1}{2}}, x_{j+\frac{1}{2}}]$ with $x_{j+\frac{1}{2}} - x_{j-\frac{1}{2}} \equiv \Delta x$ centered at $x_j = (x_{j-\frac{1}{2}} + x_{j+\frac{1}{2}})/2$ and denote by $\overline{\mathbf{U}}_j(t)$ cell averages of $\mathbf{U}(\cdot, t)$ over the corresponding intervals C_j , that is,

$$\overline{\mathbf{U}}_j(t) := \frac{1}{\Delta x} \int_{C_j} \mathbf{U}(x, t) dx.$$

We suppose that at a certain time $t \geq 0$, the point values of the computed solution $\overline{\mathbf{U}}_j(t)$ are available. Note that all of the indexed quantities are time-dependent, but from here on, we will suppress this dependence for the sake of brevity.

According to the semi-discrete LDCU scheme from [4], the computed cell averages are evolved in time by numerically solving the following system of ordinary differential equations (ODEs):

$$\frac{d\bar{\mathbf{U}}_j}{dt} = -\frac{\mathbf{F}_{j+\frac{1}{2}} - \mathbf{F}_{j-\frac{1}{2}}}{\Delta x}, \quad (2.1)$$

where $\mathbf{F}_{j+\frac{1}{2}}$ are the LDCU numerical fluxes defined by

$$\mathbf{F}_{j+\frac{1}{2}} = \frac{a_{j+\frac{1}{2}}^+ \mathbf{F}_{j+\frac{1}{2}}^- - a_{j+\frac{1}{2}}^- \mathbf{F}_{j+\frac{1}{2}}^+}{a_{j+\frac{1}{2}}^+ - a_{j+\frac{1}{2}}^-} + \frac{a_{j+\frac{1}{2}}^+ a_{j+\frac{1}{2}}^-}{a_{j+\frac{1}{2}}^+ - a_{j+\frac{1}{2}}^-} \left(\mathbf{U}_{j+\frac{1}{2}}^+ - \mathbf{U}_{j+\frac{1}{2}}^- \right) + \mathbf{q}_{j+\frac{1}{2}}.$$

Here, $\mathbf{F}_{j+\frac{1}{2}}^\pm := \mathbf{F}(\mathbf{U}_{j+\frac{1}{2}}^\pm)$ and $\mathbf{U}_{j+\frac{1}{2}}^\pm$ are the right/left-sided point values of \mathbf{U} at the cell interface $x = x_{j+\frac{1}{2}}$. The point values $\mathbf{U}_{j+\frac{1}{2}}^\pm$ are reconstructed out of the given set of cell averages $\{\bar{\mathbf{U}}_j\}$ using a proper nonlinear limiter; see §2.1.1. The one-sided local speeds of propagation $a_{j+\frac{1}{2}}^\pm$ are estimated using the largest and the smallest eigenvalues of the Jacobian $A(\mathbf{U}) := \frac{\partial \mathbf{F}}{\partial \mathbf{U}}(\mathbf{U})$, $\lambda_1(A(\mathbf{U})) \leq \dots \leq \lambda_d(A(\mathbf{U}))$. This can be done, for example, by taking

$$\begin{aligned} a_{j+\frac{1}{2}}^+ &= \max \{ \lambda_d(A(\mathbf{U}_{j+\frac{1}{2}}^+)), \lambda_d(A(\mathbf{U}_{j+\frac{1}{2}}^-)), 0 \}, \\ a_{j+\frac{1}{2}}^- &= \min \{ \lambda_1(A(\mathbf{U}_{j+\frac{1}{2}}^+)), \lambda_1(A(\mathbf{U}_{j+\frac{1}{2}}^-)), 0 \}. \end{aligned}$$

Finally, $\mathbf{q}_{j+\frac{1}{2}}$ is a built-in “anti-diffusion” term, which can be derived for a particular system at hand. For instance, we consider the 1-D Euler equations of gas dynamics, which read as (1.1) with

$$\mathbf{U} = (\rho, \rho u, E)^\top \quad \text{and} \quad \mathbf{F} = (\rho u, \rho u^2 + p, u(E + p))^\top. \quad (2.2)$$

Here, ρ , u , p , and E are the density, velocity, pressure, and total energy, respectively, and the system is completed through the following equations of state (EOS) for ideal gases:

$$p = (\gamma - 1) \left[E - \frac{1}{2} \rho u^2 \right], \quad (2.3)$$

where the parameter γ represents the specific heat ratio. For the Euler system (1.1), (2.2), (2.3), the “anti-diffusion” term $\mathbf{q}_{j+\frac{1}{2}}$ has been rigorously derived in [4,29] and it is given by

$$\mathbf{q}_{j+\frac{1}{2}} = \alpha_{j+\frac{1}{2}}^* q_{j+\frac{1}{2}}^\rho \begin{pmatrix} 1 \\ u_{j+\frac{1}{2}}^* \\ \frac{1}{2} (u_{j+\frac{1}{2}}^*)^2 \end{pmatrix}$$

with

$$q_{j+\frac{1}{2}}^\rho = \minmod \left((u_{j+\frac{1}{2}}^* - a_{j+\frac{1}{2}}^-)(\rho_{j+\frac{1}{2}}^* - \rho_{j+\frac{1}{2}}^-), (a_{j+\frac{1}{2}}^* - u_{j+\frac{1}{2}}^*)(\rho_{j+\frac{1}{2}}^* - \rho_{j+\frac{1}{2}}^-) \right), \quad u_{j+\frac{1}{2}}^* = \frac{(\rho u)^*_{j+\frac{1}{2}}}{\rho_{j+\frac{1}{2}}^*},$$

$\rho_{j+\frac{1}{2}}^*$ and $(\rho u)^*_{j+\frac{1}{2}}$ being the first and second components of

$$\mathbf{U}_{j+\frac{1}{2}}^* = \frac{a_{j+\frac{1}{2}}^+ \mathbf{U}_{j+\frac{1}{2}}^+ - a_{j+\frac{1}{2}}^- \mathbf{U}_{j+\frac{1}{2}}^- - [\mathbf{F}(\mathbf{U}_{j+\frac{1}{2}}^+) - \mathbf{F}(\mathbf{U}_{j+\frac{1}{2}}^-)]}{a_{j+\frac{1}{2}}^+ - a_{j+\frac{1}{2}}^-},$$

$$\alpha_{j+\frac{1}{2}}^* = \begin{cases} \frac{a_{j+\frac{1}{2}}^+}{a_{j+\frac{1}{2}}^+ - u_{j+\frac{1}{2}}^*} & \text{if } u_{j+\frac{1}{2}}^* < 0, \\ \frac{a_{j+\frac{1}{2}}^-}{a_{j+\frac{1}{2}}^- - u_{j+\frac{1}{2}}^*} & \text{and } \minmod(a, b) := \frac{\operatorname{sgn}(a) + \operatorname{sgn}(b)}{2} \min(|a|, |b|). \\ \frac{a_{j+\frac{1}{2}}^-}{a_{j+\frac{1}{2}}^- - u_{j+\frac{1}{2}}^*} & \text{otherwise,} \end{cases}$$

2.1.1. Nonlinear limiters

As mentioned before, the point values $\mathbf{U}_{j+\frac{1}{2}}^\pm$ are obtained with the help of a conservative piecewise linear reconstruction, designed using a proper nonlinear limiter. In this paper, we use a family of the SBM limiters (introduced in [32]) applied to the local charac-

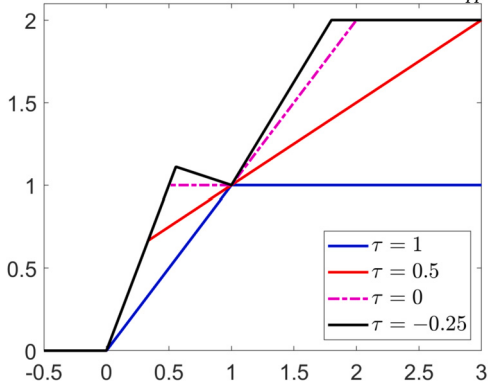


Fig. 2.1. Sketch of the family of SBM limiters ($\phi_{\theta,\tau}^{\text{SBM}}$ as functions of r) for $\theta = 2$ and $\tau = 1, 0.5, 0$, and -0.25 .

teristic variables. To this end, we introduce the matrices $\hat{A}_{j+\frac{1}{2}} = A((\bar{U}_j + \bar{U}_{j+1})/2)$ and compute the matrices $R_{j+\frac{1}{2}}$ and $R_{j+\frac{1}{2}}^{-1}$ such that $R_{j+\frac{1}{2}}^{-1} \hat{A}_{j+\frac{1}{2}} R_{j+\frac{1}{2}}$ are diagonal matrices. We then introduce the local characteristic variables Γ in the neighborhood of $x = x_{j+\frac{1}{2}}$:

$$\Gamma_k = R_{j+\frac{1}{2}}^{-1} \bar{U}_k, \quad k = j-1, j, j+1, j+2.$$

Equipped with the values Γ_{j-1} , Γ_j , Γ_{j+1} , and Γ_{j+2} , we compute the slopes

$$(\Gamma_x)_j = \phi_{\theta,\tau}^{\text{SBM}} \left(\frac{\Gamma_{j+1} - \Gamma_j}{\Gamma_j - \Gamma_{j-1}} \right) \frac{\Gamma_j - \Gamma_{j-1}}{\Delta x} \quad (2.4)$$

and

$$(\Gamma_x)_{j+1} = \phi_{\theta,\tau}^{\text{SBM}} \left(\frac{\Gamma_{j+2} - \Gamma_{j+1}}{\Gamma_{j+1} - \Gamma_j} \right) \frac{\Gamma_{j+1} - \Gamma_j}{\Delta x}, \quad (2.5)$$

where the two-parameter SBM function

$$\phi_{\theta,\tau}^{\text{SBM}}(r) := \begin{cases} 0 & \text{if } r < 0, \\ \min\{r\theta, 1 + \tau(r-1)\} & \text{if } 0 < r \leq 1, \\ r\phi_{\theta,\tau}^{\text{SBM}}(\frac{1}{r}) & \text{otherwise,} \end{cases} \quad (2.6)$$

is applied in the component-wise manner.

The parameters $\theta \in [1, 2]$ and τ in (2.6) can be used to control the amount of numerical dissipation present in the resulting scheme. First, larger θ 's correspond to less dissipative but, in general, more oscillatory reconstructions. In all of the numerical examples reported in §4, we have taken $\theta = 2$. Second, according to [32], if $\tau \geq 0.5$, then the SBM limiter is dissipative and its use typically causes contact discontinuities to be severely smeared in time. If $0 \leq \tau < 0.5$, then the SBM limiter is compressive and in this case, contact waves are usually resolved sharply within few points, but smooth extrema might be slightly compressed resulting in continuous solution profiles having a kink. If $\tau < 0$, then the limiter is overcompressive so that contact discontinuities typically stay very sharp for long time, while smooth solutions become overcompressed as time evolves resulting in the appearance of artificial $\mathcal{O}(1)$ jump discontinuities. In Fig. 2.1, we plot several $\phi_{\theta,\tau}^{\text{SBM}}$ as functions of r for $\theta = 2$ and $\tau = 1, 0.5, 0$, and -0.25 , where one can see that the effects of dissipation, compression, and overcompression are clearly distinguishable. For more details, we refer the reader to [32].

Equipped with (2.4) and (2.5), we evaluate

$$\Gamma_{j+\frac{1}{2}}^- = \Gamma_j + \frac{\Delta x}{2}(\Gamma_x)_j \quad \text{and} \quad \Gamma_{j+\frac{1}{2}}^+ = \Gamma_{j+1} - \frac{\Delta x}{2}(\Gamma_x)_{j+1},$$

and then obtain the corresponding point values of U by

$$U_{j+\frac{1}{2}}^\pm = R_{j+\frac{1}{2}} \Gamma_{j+\frac{1}{2}}^\pm.$$

Remark 2.1. For detailed explanations on how the matrices $R_{j+\frac{1}{2}}$ and $R_{j+\frac{1}{2}}^{-1}$ are computed in the case of the Euler equation of gas dynamics, we refer the reader to [3, Appendix A].

2.2. One-dimensional adaptive schemes

We now turn to the description of the proposed adaptive schemes. The key ingredient of the new schemes is the use of the different limiters from the family (2.6) in different parts of the computational domain. In particular, we use an overcompressive limiter with $\tau = -0.25$ in the “rough” parts of the computed solution and a dissipative limiter with $\tau = 0.5$ elsewhere. The latter limiter is, in fact, the Minmod2 limiter, which can be written in a simpler form since (2.4) and (2.5) with $\theta = 2$ and $\tau = 0.5$ reduce to

$$(\Gamma_x)_j = \text{minmod} \left(2 \frac{\Gamma_j - \Gamma_{j-1}}{\Delta x}, \frac{\Gamma_{j+1} - \Gamma_{j-1}}{2\Delta x}, 2 \frac{\Gamma_{j+1} - \Gamma_j}{\Delta x} \right),$$

and

$$(\Gamma_x)_{j+1} = \text{minmod} \left(2 \frac{\Gamma_{j+1} - \Gamma_j}{\Delta x}, \frac{\Gamma_{j+2} - \Gamma_j}{2\Delta x}, 2 \frac{\Gamma_{j+2} - \Gamma_{j+1}}{\Delta x} \right).$$

In order to implement this simple scheme adaption approach, we need to automatically detect “rough” parts of the computed solution. This is done using the SI proposed in [34]. This SI is based on the quantities

$$\mathcal{E}_j = \frac{|\bar{\rho}_{j+1} - 2\bar{\rho}_j + \bar{\rho}_{j-1}|}{|\bar{\rho}_{j+1} - \bar{\rho}_j| + |\bar{\rho}_j - \bar{\rho}_{j-1}| + \epsilon[|\bar{\rho}_{j+1}| + 2|\bar{\rho}_j| + |\bar{\rho}_{j-1}|]} \quad (2.7)$$

which we average in the following way:

$$\bar{\mathcal{E}}_j = \frac{1}{6} [\mathcal{E}_{j+1} + 4\mathcal{E}_j + \mathcal{E}_{j-1}].$$

Note that both $0 \leq \mathcal{E}_j < 1$ and $0 \leq \bar{\mathcal{E}}_j < 1$.

Remark 2.2. According to [34], the term with ϵ plays the role of a “noise” filter, which is added in order not to refine “wiggles” or “ripples” that may appear due to loss of monotonicity. The value of ϵ depends on the problem at hand.

We use the following simple strategy for the automatic detection of “rough” parts of the computed solution $\{\bar{\mathbf{U}}_j\}$: We mark the cell C_j as “rough” as long as

$$\bar{\mathcal{E}}_j > C,$$

where C is a positive tunable constant to be selected for each problem at hand. The robustness of this shock detection strategy depends on the sensitivity of the proposed algorithm to the choice of C . We tune C on a coarse mesh and then use the same value for fine mesh computations. Such tuning process is demonstrated in Example 1 in §4.

In general, finding an optimal C may be a very delicate task. However, our numerical experiments suggest that this tuning approach is reliable and the resulting scheme is both highly accurate and robust.

3. Two-dimensional scheme adaption algorithm

In this section, we extend the 1-D adaptive strategy introduced in §2 to the 2-D hyperbolic systems of conservation laws (1.2).

3.1. 2-D low-dissipation central-upwind (LDCU) schemes

Let the computational domain be covered with uniform cells $C_{j,k} := [x_{j-\frac{1}{2}}, x_{j+\frac{1}{2}}] \times [y_{k-\frac{1}{2}}, y_{k+\frac{1}{2}}]$ with $x_{j+\frac{1}{2}} - x_{j-\frac{1}{2}} \equiv \Delta x$ and $y_{k+\frac{1}{2}} - y_{k-\frac{1}{2}} \equiv \Delta y$ centered at (x_j, y_k) with $x_j = (x_{j-\frac{1}{2}} + x_{j+\frac{1}{2}})/2$ and $y_k = (y_{k-\frac{1}{2}} + y_{k+\frac{1}{2}})/2$. We assume that the cell averages,

$$\bar{\mathbf{U}}_{j,k} := \frac{1}{\Delta x \Delta y} \iint_{C_{j,k}} \mathbf{U}(x, y, t) dy dx,$$

have been computed at a certain time $t \geq 0$.

According to the semi-discrete LDCU scheme from [4], the computed cell averages are evolved in time by numerically solving the following system of ODEs:

$$\frac{d\bar{\mathbf{U}}_{j,k}}{dt} = -\frac{\mathcal{F}_{j+\frac{1}{2},k} - \mathcal{F}_{j-\frac{1}{2},k}}{\Delta x} - \frac{\mathcal{G}_{j,k+\frac{1}{2}} - \mathcal{G}_{j,k-\frac{1}{2}}}{\Delta y}, \quad (3.1)$$

where $\mathcal{F}_{j+\frac{1}{2},k} = \mathcal{F}_{j+\frac{1}{2},k}(\mathbf{U}_{j+\frac{1}{2},k}^-, \mathbf{U}_{j+\frac{1}{2},k}^+)$ and $\mathcal{G}_{j,k+\frac{1}{2}} = \mathcal{G}_{j,k+\frac{1}{2}}(\mathbf{U}_{j,k+\frac{1}{2}}^-, \mathbf{U}_{j,k+\frac{1}{2}}^+)$ are the LDCU numerical fluxes defined by

$$\begin{aligned}\mathbf{F}_{j+\frac{1}{2},k} &= \frac{a_{j+\frac{1}{2},k}^+ \mathbf{F}_{j+\frac{1}{2},k}^- - a_{j+\frac{1}{2},k}^- \mathbf{F}_{j+\frac{1}{2},k}^+}{a_{j+\frac{1}{2},k}^+ - a_{j+\frac{1}{2},k}^-} + \frac{a_{j+\frac{1}{2},k}^+ a_{j+\frac{1}{2},k}^-}{a_{j+\frac{1}{2},k}^+ - a_{j+\frac{1}{2},k}^-} \left[\mathbf{U}_{j+\frac{1}{2},k}^+ - \mathbf{U}_{j+\frac{1}{2},k}^- \right] + \mathbf{q}_{j+\frac{1}{2},k}^x, \\ \mathbf{G}_{j,k+\frac{1}{2}} &= \frac{b_{j,k+\frac{1}{2}}^+ \mathbf{G}_{j,k+\frac{1}{2}}^- - b_{j,k+\frac{1}{2}}^- \mathbf{G}_{j,k+\frac{1}{2}}^+}{b_{j,k+\frac{1}{2}}^+ - b_{j,k+\frac{1}{2}}^-} + \frac{b_{j,k+\frac{1}{2}}^+ b_{j,k+\frac{1}{2}}^-}{b_{j,k+\frac{1}{2}}^+ - b_{j,k+\frac{1}{2}}^-} \left[\mathbf{U}_{j,k+\frac{1}{2}}^- - \mathbf{U}_{j,k+\frac{1}{2}}^+ \right] + \mathbf{q}_{j,k+\frac{1}{2}}^y.\end{aligned}$$

Here, $\mathbf{F}_{j+\frac{1}{2},k}^\pm := \mathbf{F}(\mathbf{U}_{j+\frac{1}{2},k}^\pm)$ and $\mathbf{G}_{j,k+\frac{1}{2}}^\pm := \mathbf{G}(\mathbf{U}_{j,k+\frac{1}{2}}^\pm)$, and $\mathbf{U}_{j+\frac{1}{2},k}^\pm$ and $\mathbf{U}_{j,k+\frac{1}{2}}^\pm$ are the one-sided point values of \mathbf{U} at the cell interfaces $(x_{j+\frac{1}{2}}, y_k)$ and $(x_j, y_{k+\frac{1}{2}})$, respectively. We reconstruct the point values $\mathbf{U}_{j+\frac{1}{2},k}^\pm$ and $\mathbf{U}_{j,k+\frac{1}{2}}^\pm$ using the LCD; see Appendix A for details. The one-sided local speeds of propagation in the x - and y -directions, $a_{j+\frac{1}{2},k}^\pm$ and $b_{j,k+\frac{1}{2}}^\pm$, can be estimated by the largest and smallest eigenvalues of the Jacobians $A(\mathbf{U}) := \frac{\partial \mathbf{F}}{\partial \mathbf{U}}(\mathbf{U})$ and $B(\mathbf{U}) := \frac{\partial \mathbf{G}}{\partial \mathbf{U}}(\mathbf{U})$, for example, by setting

$$\begin{aligned}a_{j+\frac{1}{2},k}^+ &= \max \left\{ \lambda_d(A(\mathbf{U}_{j+\frac{1}{2},k}^+)), \lambda_d(A(\mathbf{U}_{j+\frac{1}{2},k}^-)), 0 \right\}, \\ a_{j+\frac{1}{2},k}^- &= \min \left\{ \lambda_1(A(\mathbf{U}_{j+\frac{1}{2},k}^+)), \lambda_1(A(\mathbf{U}_{j+\frac{1}{2},k}^-)), 0 \right\}, \\ b_{j,k+\frac{1}{2}}^+ &= \max \left\{ \lambda_d(B(\mathbf{U}_{j,k+\frac{1}{2}}^+)), \lambda_d(B(\mathbf{U}_{j,k+\frac{1}{2}}^-)), 0 \right\}, \\ b_{j,k+\frac{1}{2}}^- &= \min \left\{ \lambda_1(B(\mathbf{U}_{j,k+\frac{1}{2}}^+)), \lambda_1(B(\mathbf{U}_{j,k+\frac{1}{2}}^-)), 0 \right\}.\end{aligned}$$

Finally, $\mathbf{q}_{j+\frac{1}{2},k}^x$ and $\mathbf{q}_{j,k+\frac{1}{2}}^y$ are built-in “anti-diffusion” terms, which can be derived for a particular system (1.2) at hand. For instance, we consider the 2-D Euler equations of gas dynamics, which read as (1.2) with

$$\mathbf{U} = (\rho, \rho u, \rho v, E)^\top, \quad \mathbf{F} = (\rho u, \rho u^2 + p, \rho uv, u(E + p))^\top, \quad \mathbf{G} = (\rho v, \rho uv, \rho v^2 + p, v(E + p))^\top, \quad (3.2)$$

where v is the y -velocity and the other variables are as the same as in (2.2). The system (3.2) is completed through the following EOS for ideal gases:

$$p = (\gamma - 1) \left[E - \frac{\rho}{2}(u^2 + v^2) \right]. \quad (3.3)$$

For the sake of brevity, we omit the details on the built-in “anti-diffusion” terms $\mathbf{q}_{j+\frac{1}{2},k}^x$ and $\mathbf{q}_{j,k+\frac{1}{2}}^y$. For the system (1.2), (3.2)–(3.3), they have been derived in [4,29].

3.2. Two-dimensional adaptive schemes

We now turn to the description of the proposed adaptive schemes for the 2-D system. As in the 1-D case, we use an overcompressive SBM limiter with $\tau = -0.25$ in the “rough” parts of the computed solution and a dissipative Minmod2 limiter elsewhere. To this end, we detect the “rough” parts of the numerical solution using the SI proposed in [34]. Its 2-D version on the Cartesian mesh is based on the quantities

$$\mathcal{E}_{j,k} = \sqrt{\frac{\mathcal{E}_{j,k}^1}{\mathcal{E}_{j,k}^2}},$$

where

$$\begin{aligned}\mathcal{E}_{j,k}^1 &= (\bar{\rho}_{j+1,k} - 2\bar{\rho}_{j,k} + \bar{\rho}_{j-1,k})^2 + (\bar{\rho}_{j,k+1} - 2\bar{\rho}_{j,k} + \bar{\rho}_{j,k-1})^2, \\ \mathcal{E}_{j,k}^2 &= (|\bar{\rho}_{j+1,k} - \bar{\rho}_{j,k}| + |\bar{\rho}_{j,k} - \bar{\rho}_{j-1,k}| + \epsilon [|\bar{\rho}_{j+1,k}| + 2|\bar{\rho}_{j,k}| + |\bar{\rho}_{j-1,k}|])^2 \\ &\quad + (|\bar{\rho}_{j,k+1} - \bar{\rho}_{j,k}| + |\bar{\rho}_{j,k} - \bar{\rho}_{j,k-1}| + \epsilon [|\bar{\rho}_{j,k+1}| + 2|\bar{\rho}_{j,k}| + |\bar{\rho}_{j,k-1}|])^2,\end{aligned} \quad (3.4)$$

with ϵ playing the role of a “noise” filter; see Remark 2.2. The desired SI is then obtained using a proper averaging, for instance, by

$$\begin{aligned}\bar{\mathcal{E}}_{j,k} &= \frac{1}{36} [\mathcal{E}_{j-1,k-1} + \mathcal{E}_{j-1,k+1} + \mathcal{E}_{j+1,k-1} + \mathcal{E}_{j+1,k+1} \\ &\quad + 4(\mathcal{E}_{j-1,k} + \mathcal{E}_{j,k-1} + \mathcal{E}_{j,k+1} + \mathcal{E}_{j+1,k}) + 16\mathcal{E}_{j,k}].\end{aligned}$$

We act similarly to the 1-D case and mark the cell $C_{j,k}$ as “rough” if $\bar{\mathcal{E}}_{j,k} > C$, where C is a positive tunable constant to be selected for each problem at hand.

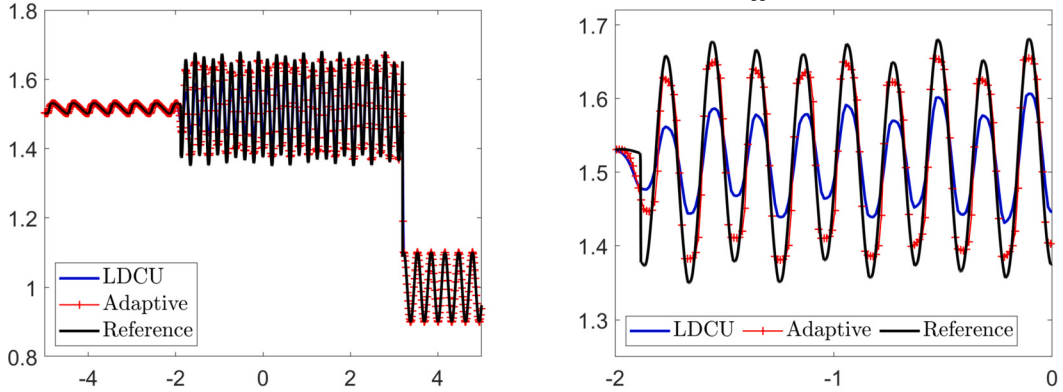


Fig. 4.1. Example 1: Density ρ computed by the original and adaptive LDCU schemes (left) and zoom at $x \in [-2, 0]$ (right).

4. Numerical examples

In this section, we test the developed adaptive schemes on several numerical examples. To this end, we compare the performance of the original and adaptive LDCU schemes by applying them to a number of initial-boundary value problems for the 1-D and 2-D Euler equations of gas dynamics.

In all of the numerical examples, we have solved the ODE systems (2.1) and (3.1) using the three-stage third-order strong stability preserving (SSP) Runge-Kutta method; see, e.g., [17, 18]. We take $\gamma = 1.4$ in Example 1–5 and $\gamma = 5/3$ in Example 6. The CFL number is 0.4 and the SI parameter ε in (2.7) and (3.4) is 0.2 in all of the examples. Note that the same value of ε was used in [34].

4.1. One-dimensional examples

Example 1—shock-entropy wave interaction problem. In the first example taken from [44], we consider the shock-entropy wave interaction problem. The initial conditions,

$$(\rho, u, p) \Big|_{(x,0)} = \begin{cases} (1.51695, 0.523346, 1.805), & x < -4.5, \\ (1 + 0.1 \sin(20x), 0, 1), & x > -4.5, \end{cases}$$

correspond to a forward-facing shock wave of Mach number 1.1 interacting with high-frequency density perturbations, that is, as the shock wave moves, the perturbations spread ahead. We set the free boundary condition at the both ends of the computational domain $[-5, 5]$.

We compute the numerical solution until the final time $t = 5$ by the original and adaptive LDCU schemes on a uniform mesh with $\Delta x = 1/80$. We use the adaption constant $C = 0.01$ in the adaptive LDCU scheme. The numerical results at time $t = 5$ are presented in Fig. 4.1 along with the reference solution computed by the adaptive LDCU scheme on a much finer mesh with $\Delta x = 1/1600$. In Fig. 4.1 (right), we zoom the obtained solutions at the interval $[-2, 0]$, at which the exact solution is smooth but has an oscillatory nature. As one can see, this part of the solution is resolved much more accurately by the adaptive scheme.

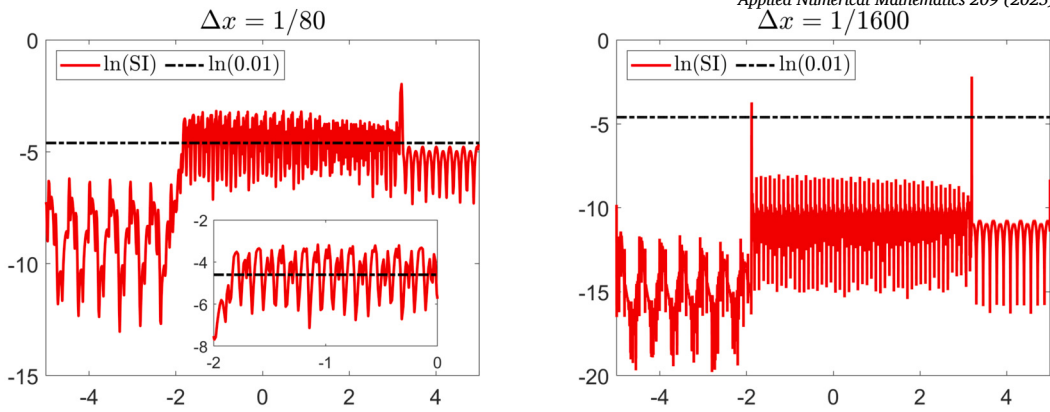
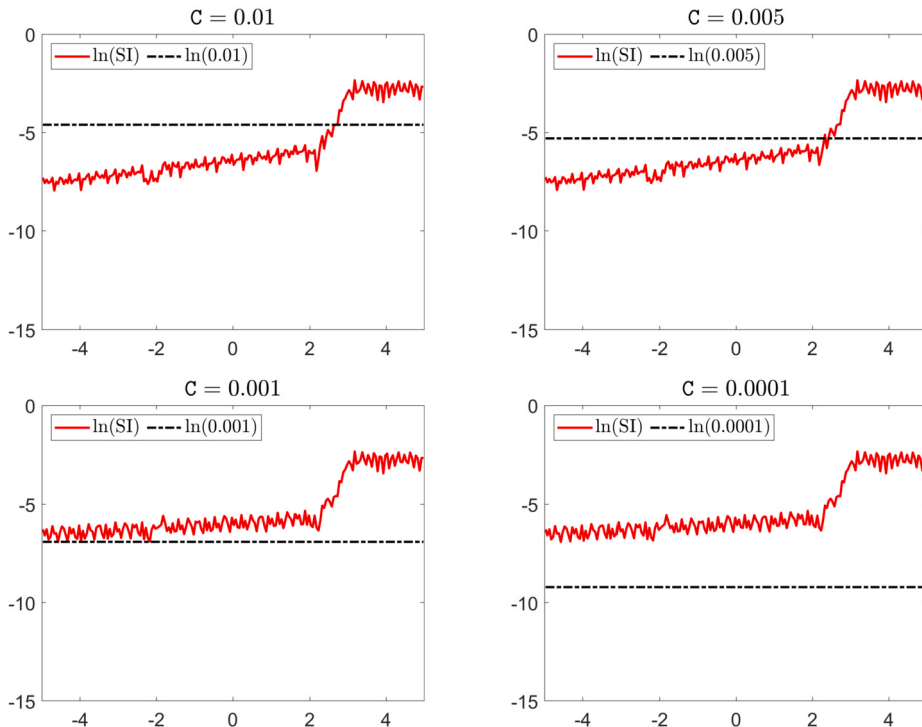
We also plot $\ln(\bar{\mathcal{E}}_j)$ computed on coarse and fine uniform meshes with $\Delta x = 1/80$ and $1/1600$, respectively; see Fig. 4.2. One can observe that on the coarse mesh the values of the SI are larger than threshold value 0.01 not only at the shock region but also near the local extrema, where the overcompressive SBM limiter is used. This helps to significantly improve the resolution of these parts of the computed solution. At the same time, when the mesh is refined, the SI starts detecting only the shock areas as “rough” ones and hence no staircase-like overcompressed structures are observed.

In order to show how to tune the threshold C , we adopt the approach proposed in [19]: for the problem at hand, the coefficient C is first adjusted on coarse grids (this makes the tuning process computationally inexpensive) and then used for high-resolution computation on finer grids. In this example, we first compute the numerical results on the coarse mesh with $\Delta x = 1/20$ with $C = 0.005, 0.01, 0.001, 0.0001$ and plot the corresponding $\ln(\bar{\mathcal{E}}_j)$ in Fig. 4.3. We then compute the corresponding numerical results on a finer mesh with $\Delta x = 1/200$ and plot the obtained numerical results in Fig. 4.4. One can see that if $\bar{\mathcal{E}}_j > C$ in the smooth areas in the coarse-mesh computation, then there will be staircase-like structures in the corresponding fine-mesh solution.

Example 2—shock-density wave interaction problem. In the second example taken from [45], we consider the shock-density wave interaction problem. The initial data,

$$(\rho, u, p) \Big|_{(x,0)} = \begin{cases} \left(\frac{27}{7}, \frac{4\sqrt{35}}{9}, \frac{31}{3}\right), & x < -4, \\ (1 + 0.2 \sin(5x), 0, 1), & x > -4, \end{cases}$$

are prescribed in the computational domain $[-5, 15]$ subject to the free boundary conditions.

Fig. 4.2. Example 1: $\ln(\text{SI})$ computed with $\Delta x = 1/80$ (left) and $1/1600$ (right).Fig. 4.3. Example 1: $\ln(\text{SI})$ computed with $\Delta x = 1/20$ and $C = 0.01$ (top left), $C = 0.005$ (top right), $C = 0.001$ (bottom left), and $C = 0.0001$ (bottom right).

We compute the numerical solutions by the original and adaptive LDCU schemes on a uniform mesh with $\Delta x = 1/40$ until the final time $t = 5$. The adaptive LDCU scheme is used with the adaption constant $C = 0.01$. We present the obtained numerical results in Fig. 4.5 together with the reference solution computed by the adaptive LDCU scheme on a much finer mesh with $\Delta x = 1/400$. It can be clearly seen in Fig. 4.5 (right) that the adaptive LDCU scheme produces more accurate result compared to that obtained by the original LDCU scheme.

Example 3—blast wave problem. In the last 1-D example, we consider a strong shocks interaction problem from [55], which is considered on the interval $[0, 1]$ with the solid wall boundary conditions at both ends and subject to the following initial conditions:

$$(\rho, u, p)|_{(x,0)} = \begin{cases} (1, 0, 1000), & x < 0.1, \\ (1, 0, 0.01), & 0.1 \leq x \leq 0.9, \\ (1, 0, 100), & x > 0.9. \end{cases}$$

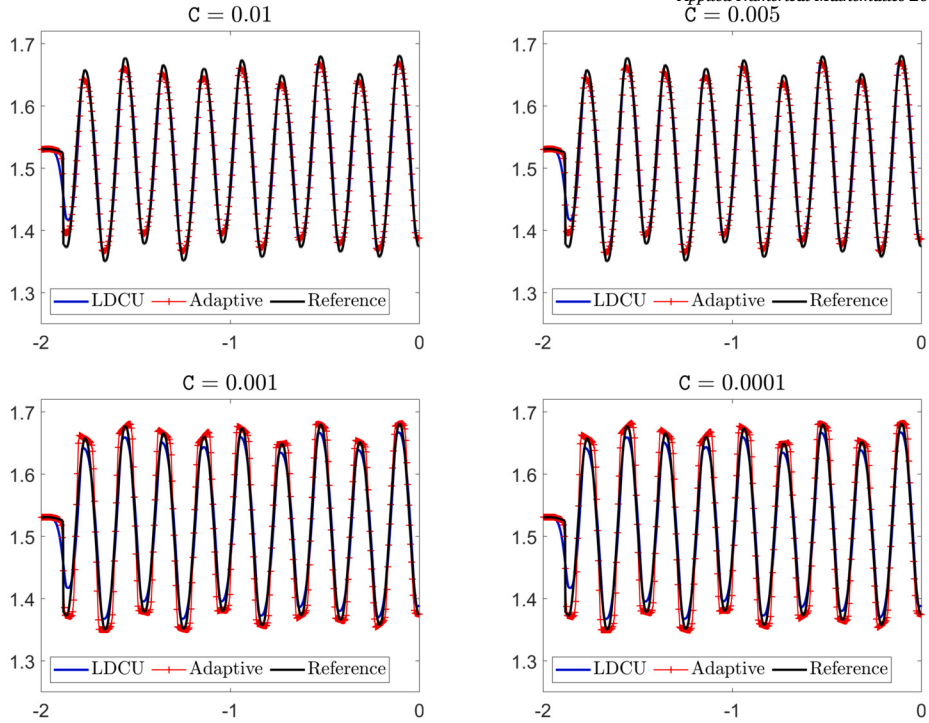


Fig. 4.4. Example 1: Density ρ (zoom at $x \in [-2, 0]$) computed with $\Delta x = 1/200$ and $C = 0.01$ (top left), $C = 0.005$ (top right), $C = 0.001$ (bottom left), and $C = 0.0001$ (bottom right).

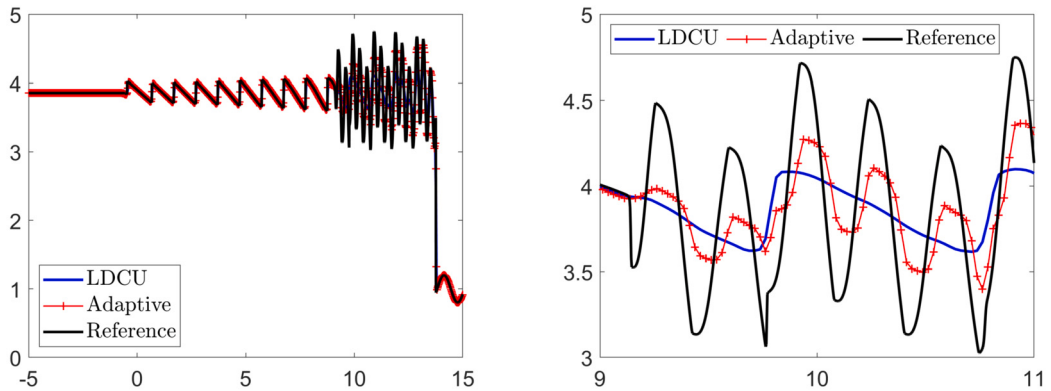


Fig. 4.5. Example 2: Density ρ computed by the original and adaptive LDCU schemes (left) and zoom at $x \in [11.8, 13.6]$ (right).

We compute the numerical solutions until the final time $t = 0.038$ by the original and adaptive (with the adaption constant $C = 0.01$) LDCU schemes on a uniform mesh with $\Delta x = 1/400$ and use the adaptive LDCU scheme on a much finer grid with $\Delta x = 1/8000$ to compute the reference solution.

In addition, we compute the numerical solution on the same mesh, but by the adaptive LDCU scheme that uses a different SI to detect “rough” parts of the computed solution. To this end, we implement the Minmod-based SI (the resulting adaptive scheme will be referred to as MM-adaptive LDCU scheme), which is taken from [53] and is computed as follows. We first compute the Minmod-based quantities

$$s_j = \text{minmod}\{\bar{\rho}_{j+1} - \bar{\rho}_j, \bar{\rho}_j - \bar{\rho}_{j-1}\},$$

and then we say that the cell C_j is “rough” if $|s_j| > \max\{|s_{j-1}|, |s_{j+1}|\} + \delta$, where δ is a small positive number. The parameter δ has to be selected for each problem at hand and it should indicate a size of a jump in ρ , which we neglect when detecting “rough” parts of the solution. In fact, this SI is not very sensitive to the choice of δ . Here, we have taken $\delta = 10^{-4}$. We refer the readers to [53] for more details of the Minmod-based SI.

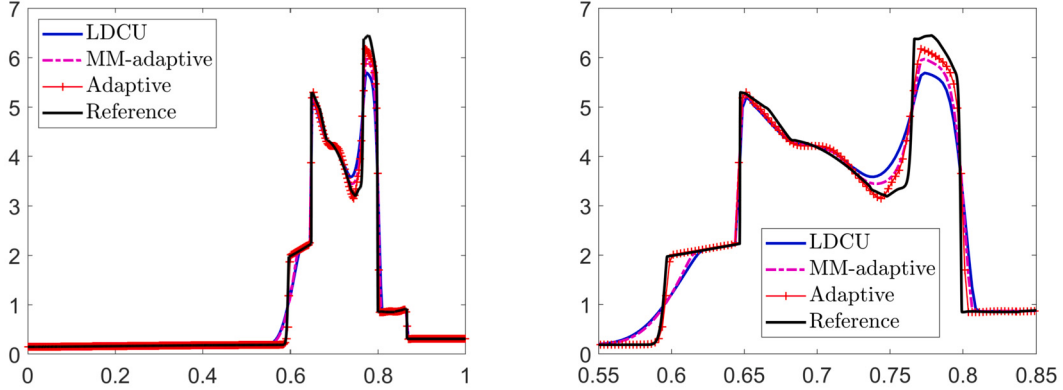


Fig. 4.6. Example 3: Density ρ computed by the original, adaptive, and MM-adaptive LDCU schemes (left) and zoom at $x \in [0.55, 0.85]$.

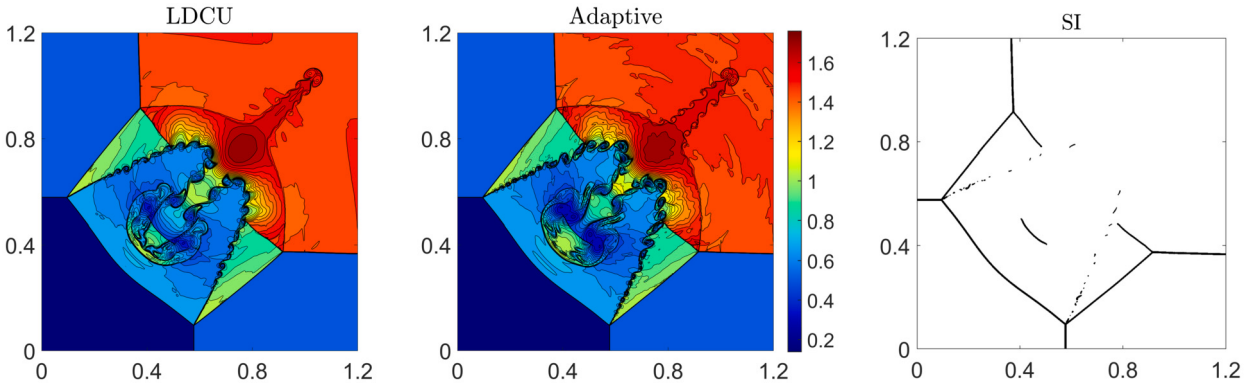


Fig. 4.7. Example 4: Density ρ computed by the original (left), adaptive (middle) LDCU schemes, and the “rough” areas detected by the SI (right).

The obtained results, presented in Fig. 4.6, demonstrate that the adaptive LDCU scheme is much more accurate than the original and the MM-adaptive LDCU schemes as the adaptive LDCU scheme is capable of achieving a superb resolution of the contact wave located at about $x = 0.6$. It is well-known that this contact wave is the one, which is hardest to get sharply resolved, and the proposed adaptive LDCU scheme is, to best of our knowledge, the first Riemann-problem-solver-free scheme that can achieve this goal. We would also like to emphasize that not only the aforementioned Minmod-based SI, but all other SIs we have tested (the obtained results are not shown for the sake of brevity) were not sufficiently robust in the sense that their use in the context of the proposed LDCU scheme could not lead to so high resolution of the aforementioned contact wave.

4.2. Two-dimensional examples

Example 4—2-D Riemann problem. In the first 2-D example, we consider Configuration 3 of the 2-D Riemann problems from [28] (also see [40,41,56]) with the initial conditions

$$(\rho, u, v, p) \Big|_{(x,y,0)} = \begin{cases} (1.5, 0, 0, 1.5), & x > 1, y > 1, \\ (0.5323, 1.206, 0, 0.3), & x < 1, y > 1, \\ (0.138, 1.206, 1.206, 0.029), & x < 1, y < 1, \\ (0.5323, 0, 1.206, 0.3), & x > 1, y < 1, \end{cases}$$

prescribed in the computational domain $[0, 1.2] \times [0, 1.2]$ subject to the free boundary conditions.

We compute the numerical solution until the final time $t = 1$ by the original and adaptive (with the adaption constant $C = 0.08$) LDCU schemes on a uniform mesh with $\Delta x = \Delta y = 3/2500$ and present the obtained results in Fig. 4.7 (left and middle), where one can see that the adaptive LDCU scheme outperforms the original LDCU scheme in capturing a sideband instability of the jet in the zones of strong along-jet velocity shear and the instability along the jets neck. In Fig. 4.7 (right), we show the regions which have been detected as “rough” by the SI at the final time. As one can see, when the adaptive LDCU scheme is used, a sharper SBM limiter is implemented only in a small part of the computational domain.

In order to illustrate how sensitive the adaptive algorithm is to the selection of the threshold C , we compute the solution using the adaptive LDCU scheme with three different threshold values $C = 0.1, 0.2$, and 0.5 . We plot the obtained numerical results together with the corresponding SIs in Fig. 4.8, where one can see that the quality of the achieved resolution decreases when C grows and

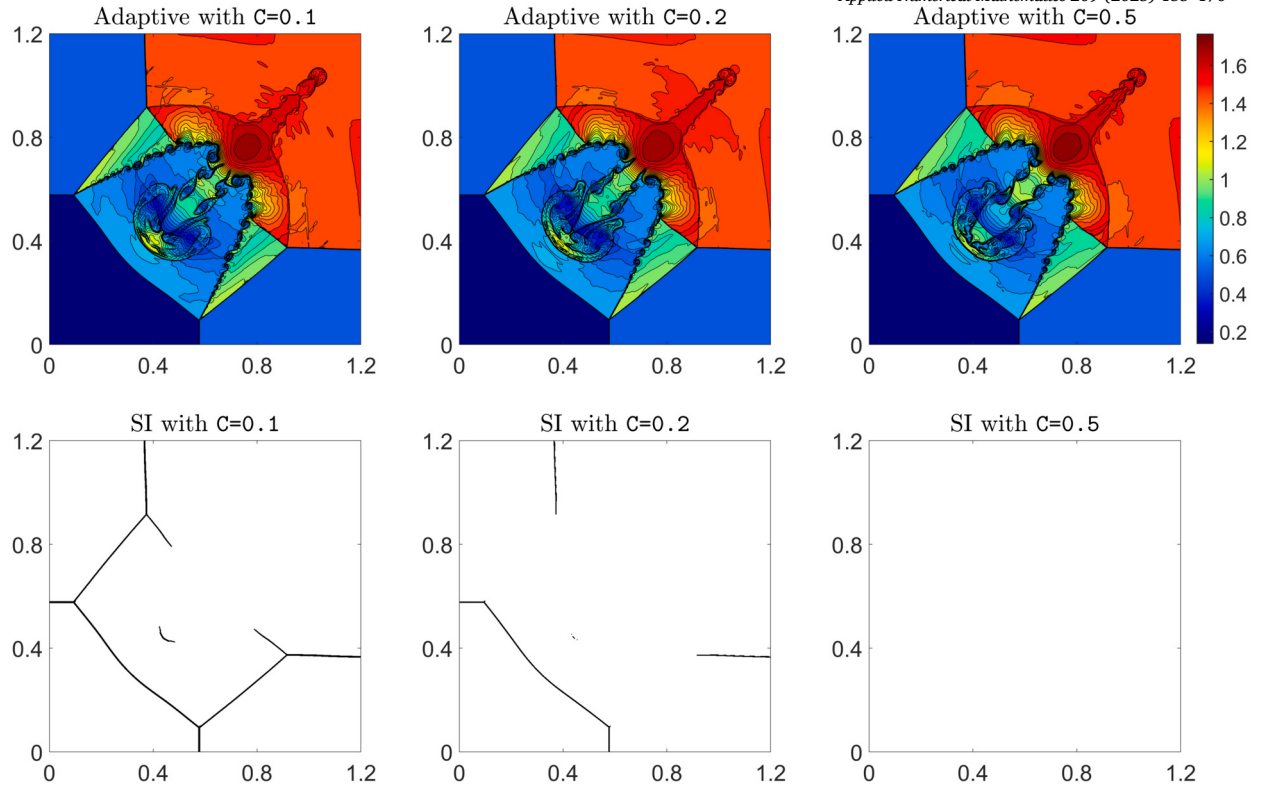


Fig. 4.8. Example 4: Density ρ computed by the adaptive LDCU scheme with different adaption constants C (top row) and the corresponding “rough” areas detected by the SI (bottom row).

when $C = 0.5$, the adaptive LDCU solution as basically the same as the non-adaptive one as (at least at the final time) no “rough” areas are detected by the SI.

Example 5—implosion problem. In this example, we consider the implosion problem taken from [33]. The initial conditions,

$$(\rho, u, v, p) \Big|_{(x,y,0)} = \begin{cases} (0.125, 0, 0, 0.14), & |x| + |y| < 0.15, \\ (1, 0, 0, 1), & \text{otherwise,} \end{cases}$$

are prescribed in $[0, 0.3] \times [0, 0.3]$ with the solid wall boundary conditions imposed at all of the four sides. This example was designed to test the amount of numerical diffusion present in different schemes as there is a jet forming near the origin and propagating along the diagonal $y = x$ direction, and schemes containing large numerical diffusion may not resolve the jet at all or the jet propagation velocity may be affected by the numerical diffusion.

We compute the numerical solution until the final time $t = 2.5$ by the original and adaptive (with the adaption constant $C = 0.05$) LDCU schemes on a uniform mesh with $\Delta x = \Delta y = 3/2500$ and present the obtained numerical results in Fig. 4.9 (left and middle). As one can observe, while the jet is generated by all of the studied schemes, it propagates much further in the diagonal direction when the solution is computed by the adaptive LDCU scheme. In Fig. 4.9 (right), we show the regions which have been detected as “rough” by the SI at the final time. One can see that when the adaptive LDCU scheme is used, a sharper SBM limiter is implemented only in a small part of the computational domain.

In this example, we also check the efficiency of the proposed adaptive LDCU scheme by comparing it with the original LDCU scheme. To this end, we measure the CPU time consumed by the adaptive LDCU scheme and refine the mesh used by the original LDCU scheme to the level that exactly the same CPU time is consumed to compute both of the numerical solutions. The corresponding grids are of sizes $\Delta x = \Delta y = 3/2500$ for the adaptive LDCU scheme, and $\Delta x = \Delta y = 3/2520$ for the original LDCU scheme. The obtained finer mesh LDCU solution is plotted in Fig. 4.10 (left). One can also reduce the computational cost of the original LDCU scheme by applying the piecewise linear reconstruction to the conservative variables without using the LCD. In this case, one has to further refine the mesh up to $\Delta x = \Delta y = 3/3200$ to ensure that the same CPU is consumed. This leads to the enhanced resolution, as one can see in Fig. 4.10 (right), but it is still not as high as the one achieved by the adaptive LDCU scheme: compare this figure with Fig. 4.9 (middle). This clearly demonstrates that the adaptive LDCU scheme clearly outperforms the original one.

Example 6—RT instability. In the last example taken from [42], we investigate the RT instability, which is a physical phenomenon occurring when a layer of heavier fluid is placed on top of a layer of lighter fluid. To this end, we first modify the 2-D Euler equations

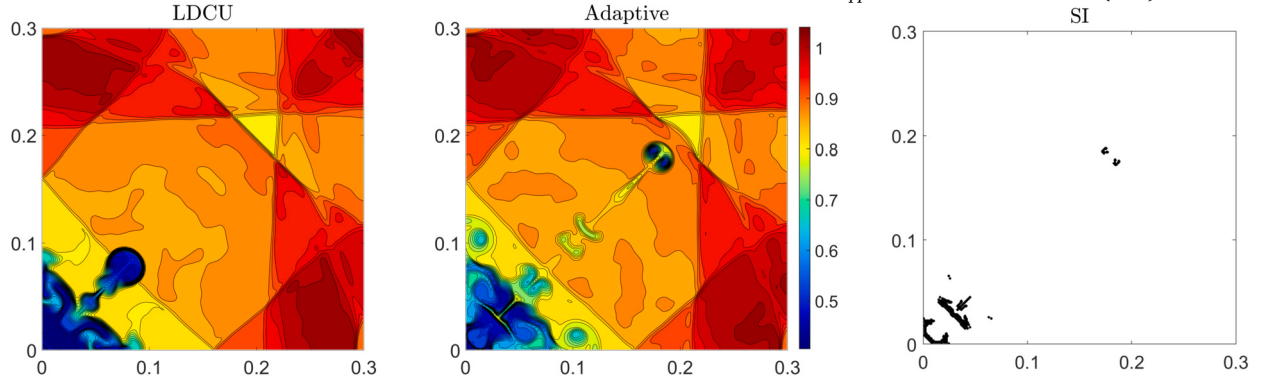


Fig. 4.9. Example 5: Density ρ computed by the original (left), adaptive (middle) LDCU schemes, and the “rough” areas detected by the SI (right).

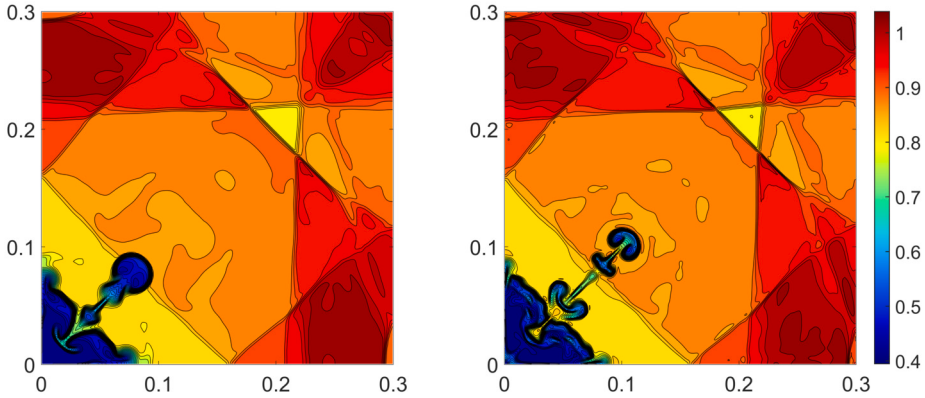


Fig. 4.10. Example 5: Density ρ computed by the original LDCU scheme using the reconstruction of the local characteristic variables and $\Delta x = \Delta y = 3/2520$ (left) and using the reconstruction of the conserved variables and with $\Delta x = \Delta y = 3/3200$ (right).

of gas dynamics (1.2), (3.2)–(3.3) by adding the gravitational source terms acting in the positive direction of the y -axis into the RHS of the system:

$$\begin{aligned} \rho_t + (\rho u)_x + (\rho v)_y &= 0, \\ (\rho u)_t + (\rho u^2 + p)_x + (\rho uv)_y &= 0, \\ (\rho v)_t + (\rho uv)_x + (\rho v^2 + p)_y &= \rho, \\ E_t + [u(E + p)]_x + [v(E + p)]_y &= \rho v, \end{aligned}$$

and then use the following initial conditions:

$$(\rho, u, v, p)|_{(x,y,0)} = \begin{cases} (2, 0, -0.025c \cos(8\pi x), 2y + 1), & y < 0.5, \\ (1, 0, -0.025c \cos(8\pi x), y + 1.5), & \text{otherwise}, \end{cases}$$

where $c := \sqrt{\gamma p / \rho}$ is the speed of sound. The solid wall boundary conditions are imposed at $x = 0$ and $x = 0.25$, and the following Dirichlet boundary conditions are specified at the top and bottom boundaries:

$$(\rho, u, v, p)(x, 1, t) = (1, 0, 0, 2.5), \quad (\rho, u, v, p)(x, 0, t) = (2, 0, 0, 1).$$

We compute the numerical solution until the final time $t = 2.95$ by the original and adaptive (with the adaption constant $C = 0.08$) LDCU schemes on a uniform mesh with $\Delta x = \Delta y = 1/1024$ in the computational domain $[0, 0.25] \times [0, 1]$, and then present the numerical results obtained at the times $t = 1.95$ and 2.95 in Fig. 4.11. As one can see, the adaptive LDCU scheme resolves more small structures than the original LDCU scheme, which again demonstrates that using a sharper SBM limiter can produce sharper numerical results. As in the previous examples, we also show the regions which have been detected as “rough” by the SI at the final time; see Fig. 4.12.

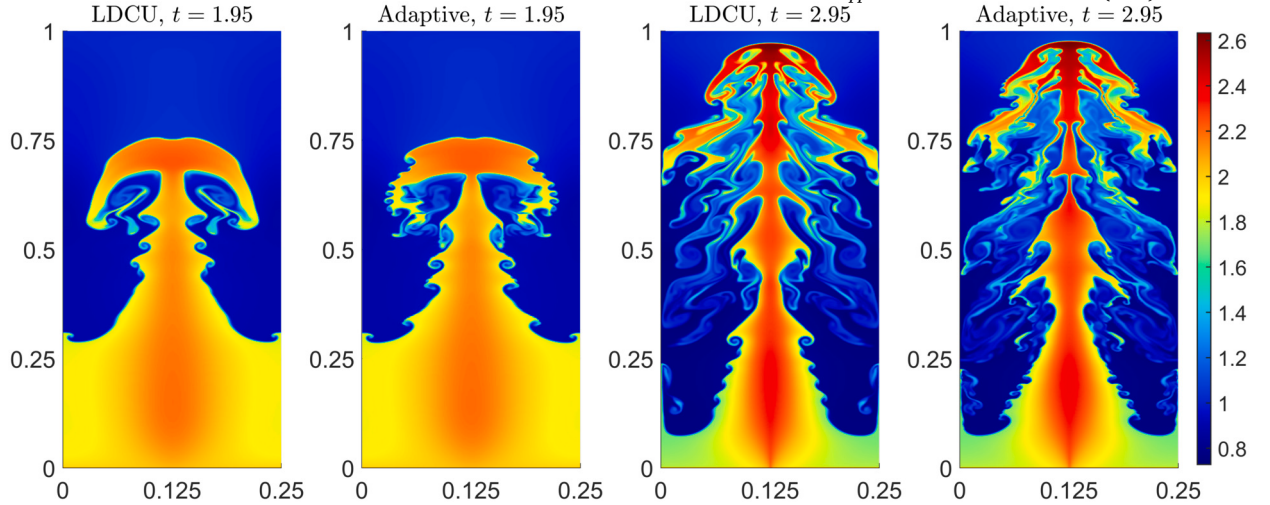


Fig. 4.11. Example 6: Density ρ computed by the original and adaptive LDCU schemes at $t = 1.95$ and 2.95 .

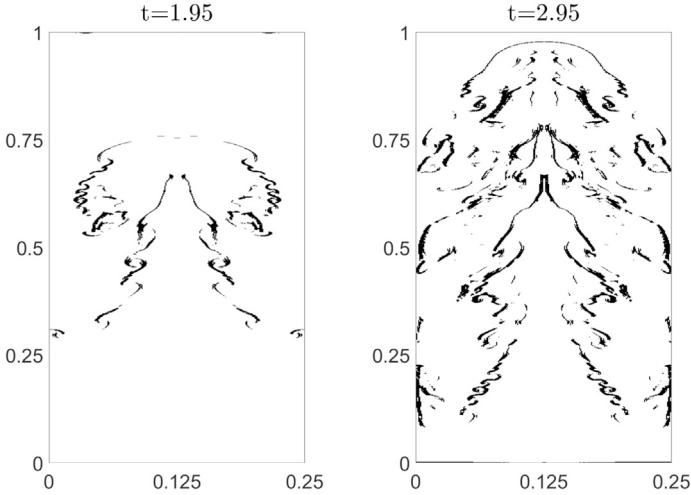


Fig. 4.12. Example 6: “Rough” areas detected by the SI at $t = 1.95$ (left) and 2.95 (right).

Remark 4.1. In this example, the solution is symmetric with respect to the vertical axis $x = 0.125$. In order to enforce this symmetry, we have applied the strategy from [51]: upon completion of each time evolution step, we replace the computed cell averages $\bar{U}_{j,k}$ with $\hat{U}_{j,k}$, where

$$\begin{aligned}\hat{\rho}_{j,k} &= \frac{\bar{\rho}_{j,k} + \bar{\rho}_{M-j,k}}{2}, & (\hat{\rho}u)_{j,k} &= \frac{(\bar{\rho}u)_{j,k} - (\bar{\rho}u)_{M-j,k}}{2}, \\ (\hat{\rho}v)_{j,k} &= \frac{(\bar{\rho}v)_{j,k} + (\bar{\rho}v)_{M-j,k}}{2}, & \hat{E}_{j,k} &= \frac{\bar{E}_{j,k} + \bar{E}_{M-j,k}}{2},\end{aligned}$$

for all $j = 1, \dots, M$ and for all k . Alternative symmetry enforcement techniques can be found in, e.g., [6,7,10,49].

In addition, we compute the Cesàro averages of the numerical solutions on meshes with different resolutions. As proved in [9], the Cesàro averages converge strongly (in the L^q -norm with $1 \leq q < \infty$) to a dissipative weak solution. In order to approximate the limiting solution, we consider the Cesàro averages of the densities computed by the original and adaptive LDCU schemes. To this end, we introduce the sequence of meshes with the cells of size $1/2^n$, $n = 5, \dots, 10$, and denote by $\rho(1/2^n)$ the density computed on the corresponding mesh. We then project the obtained coarser mesh solutions with $n = 5, \dots, m-1$ onto the finer mesh with $n = m$ (the projection is carried out using a fifth-order WENO-Z interpolation from [52] applied to the density field) and denote the obtained results still by $\rho(1/2^n)$, $n = 5, \dots, m$. After this, we compute the Cesàro averages by

$$\rho^C(1/2^m) = \frac{\rho(1/2^5) + \dots + \rho(1/2^m)}{m-4}, \quad m = 8, 9, 10.$$

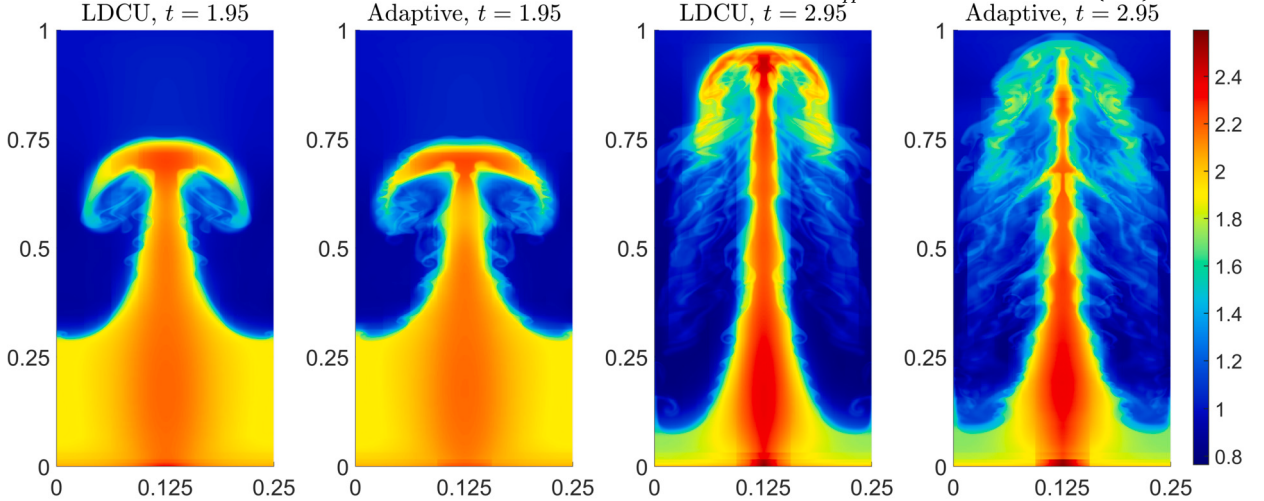


Fig. 4.13. Example 6: Cesàro averages of the density ρ^C computed by the original and adaptive LDCU schemes.

The obtained results are presented in Fig. 4.13, where one can observe the superiority of the results obtained by the adaptive LDCU scheme.

5. Conclusion

In this paper, we have introduced new second-order adaptive low-dissipation central-upwind (LDCU) schemes for the one- (1-D) and two-dimensional (2-D) hyperbolic systems of conservation laws. The new adaptive schemes are based on the recently proposed LDCU fluxes and a smoothness indicator used to automatically detect “rough” areas of the computed solutions. We then use the overcompressive SBM limiters in the “rough” areas to achieve higher resolution of the computed shocks and contact discontinues and the dissipative Minmod2 limiters elsewhere to avoid the staircase-like overcompressed structures in the smooth parts of the computed solutions. We have applied the developed adaptive LDCU schemes to the 1-D and 2-D Euler equations of gas dynamics and the obtained numerical results clearly demonstrate that the adaptive LDCU scheme outperforms the original LDCU scheme.

CRediT authorship contribution statement

Shaoshuai Chu: Writing – original draft, Visualization, Validation, Software, Methodology, Investigation, Formal analysis, Data curation, Conceptualization. **Alexander Kurganov:** Writing – original draft, Validation, Supervision, Resources, Project administration, Methodology, Investigation, Funding acquisition, Formal analysis, Data curation, Conceptualization. **Igor Menshov:** Methodology, Investigation, Formal analysis, Conceptualization.

Acknowledgements

The work of S. Chu was supported in part by the DFG (German Research Foundation) through HE5386/19-3, 27-1. The work of A. Kurganov was supported in part by NSFC grant 12171226, and by the fund of the Guangdong Provincial Key Laboratory Of Computational Science And Material Design (No. 2019B030301001).

Appendix A. 2-D LCD-based piecewise linear reconstruction

In this appendix, we describe how to reconstruct the one-sided point values $\mathbf{U}_{j+\frac{1}{2},k}^\pm$ (the point values $\mathbf{U}_{j,k+\frac{1}{2}}^\pm$ can be computed in a similar manner and we omit the details for the sake of brevity). To this end, as in the 1-D case, we first introduce the local characteristic variables in the neighborhood of $(x, y) = (x_{j+\frac{1}{2}}, y_k)$:

$$\boldsymbol{\Gamma}_{\ell,k} = R_{j+\frac{1}{2},k}^{-1} \overline{\mathbf{U}}_{\ell,k}, \quad \ell = j-1, j, j+1, j+2,$$

where the matrix $R_{j+\frac{1}{2},k}$ is such that $R_{j+\frac{1}{2},k}^{-1} \hat{\mathbf{A}}_{j+\frac{1}{2},k} R_{j+\frac{1}{2},k}$ is diagonal and a locally linearized Jacobian is $\hat{\mathbf{A}}_{j+\frac{1}{2},k} := A((\overline{\mathbf{U}}_{j,k} + \overline{\mathbf{U}}_{j+1,k})/2)$.

Equipped with the values $\boldsymbol{\Gamma}_{j-1,k}$, $\boldsymbol{\Gamma}_{j,k}$, $\boldsymbol{\Gamma}_{j+1,k}$, and $\boldsymbol{\Gamma}_{j+2,k}$, we compute

$$(\boldsymbol{\Gamma}_x)_{j,k} = \phi_{\theta,\tau}^{\text{SBM}} \left(\frac{\boldsymbol{\Gamma}_{j+1,k} - \boldsymbol{\Gamma}_{j,k}}{\boldsymbol{\Gamma}_{j,k} - \boldsymbol{\Gamma}_{j-1,k}} \right) \frac{\boldsymbol{\Gamma}_{j,k} - \boldsymbol{\Gamma}_{j-1,k}}{\Delta x},$$

and

$$(\Gamma_x)_{j+1,k} = \phi_{\theta,\tau}^{\text{SBM}} \left(\frac{\Gamma_{j+2,k} - \Gamma_{j+1,k}}{\Gamma_{j+1,k} - \Gamma_{j,k}} \right) \frac{\Gamma_{j+1,k} - \Gamma_{j,k}}{\Delta x},$$

where the SBM function, defined in (2.3), is applied in the component-wise manner. We then use these slopes to evaluate

$$\Gamma_{j+\frac{1}{2},k}^- = \Gamma_{j,k} + \frac{\Delta x}{2} (\Gamma_x)_{j,k} \quad \text{and} \quad \Gamma_{j+\frac{1}{2},k}^+ = \Gamma_{j+1,k} - \frac{\Delta x}{2} (\Gamma_x)_{j+1,k},$$

and finally obtain the corresponding point values of \mathbf{U} by

$$\mathbf{U}_{j+\frac{1}{2}}^\pm = R_{j+\frac{1}{2},k} \Gamma_{j+\frac{1}{2},k}^\pm.$$

Remark A.1. The matrices $R_{j+\frac{1}{2},k}$ and $R_{j+\frac{1}{2},k}^{-1}$ for the 2-D Euler equation of gas dynamics (3.2)–(3.3) can be found in [3, Appendix C].

References

- [1] F. Aràndiga, A. Baeza, R. Donat, Vector cell-average multiresolution based on Hermite interpolation, *Adv. Comput. Math.* 28 (2008) 1–22.
- [2] M. Ben-Artzi, J. Falcovitz, *Generalized Riemann Problems in Computational Fluid Dynamics*, Cambridge Monographs on Applied and Computational Mathematics, vol. 11, Cambridge University Press, Cambridge, 2003.
- [3] A. Chertock, S. Chu, M. Herty, A. Kurganov, M. Lukáčová-Medviďová, Local characteristic decomposition based central-upwind scheme, *J. Comput. Phys.* 473 (2023) 111718.
- [4] S. Chu, A. Kurganov, R. Xin, New low-dissipation central-upwind schemes. Part II, submitted for publication, preprint available at <https://doi.org/10.48550/arXiv.2405.07620>.
- [5] J. Dewar, A. Kurganov, M. Leopold, Pressure-based adaption indicator for compressible Euler equations, *Numer. Methods Partial Differ. Equ.* 31 (2015) 1844–1874.
- [6] W.S. Don, D.-M. Li, Z. Gao, B.-S. Wang, A characteristic-wise alternative WENO-Z finite difference scheme for solving the compressible multicomponent non-reactive flows in the overestimated quasi-conservative form, *J. Sci. Comput.* 82 (2020) 27.
- [7] W.S. Don, P. Li, K.Y. Wong, Z. Gao, Improved symmetry property of high order weighted essentially non-oscillatory finite difference schemes for hyperbolic conservation laws, *Adv. Appl. Math. Mech.* 10 (2018) 1418–1439.
- [8] M. Dumbser, O. Zanotti, R. Loubère, S. Diot, A posteriori subcell limiting of the discontinuous Galerkin finite element method for hyperbolic conservation laws, *J. Comput. Phys.* 278 (2014) 47–75.
- [9] E. Feireisl, M. Lukáčová-Medviďová, H. Mizerová, B. She, *Numerical Analysis of Compressible Fluid Flows*, MS&A. Modeling, Simulation and Applications, vol. 20, Springer, Cham, 2021.
- [10] N. Fleischmann, S. Adami, N.A. Adams, Numerical symmetry-preserving techniques for low-dissipation shock-capturing schemes, *Comput. Fluids* 189 (2019) 94–107.
- [11] K.O. Friedrichs, Symmetric hyperbolic linear differential equations, *Commun. Pure Appl. Math.* 7 (1954) 345–392.
- [12] G. Fu, C.-W. Shu, A new troubled-cell indicator for discontinuous Galerkin methods for hyperbolic conservation laws, *J. Comput. Phys.* 347 (2017) 305–327.
- [13] A. Gelb, E. Tadmor, Spectral reconstruction of piecewise smooth functions from their discrete data, *M2AN Math. Model. Numer. Anal.* 36 (2002) 155–175.
- [14] A. Gelb, E. Tadmor, Adaptive edge detectors for piecewise smooth data based on the minmod limiter, *J. Sci. Comput.* 28 (2006) 279–306.
- [15] E. Godlewski, P.-A. Raviart, *Numerical Approximation of Hyperbolic Systems of Conservation Laws*, second ed., Springer-Verlag, New York, 2021.
- [16] S.K. Godunov, A difference method for numerical calculation of discontinuous solutions of the equations of hydrodynamics, *Mat. Sb. (N.S.)* 47 (1959) 271–306.
- [17] S. Gottlieb, D. Ketcheson, C.-W. Shu, *Strong Stability Preserving Runge-Kutta and Multistep Time Discretizations*, World Scientific Publishing Co. Pte. Ltd., Hackensack, NJ, 2011.
- [18] S. Gottlieb, C.-W. Shu, E. Tadmor, Strong stability-preserving high-order time discretization methods, *SIAM Rev.* 43 (2001) 89–112.
- [19] J.-L. Guermond, R. Pasquetti, B. Popov, Entropy viscosity method for nonlinear conservation laws, *J. Comput. Phys.* 230 (2011) 4248–4267.
- [20] A. Harten, ENO schemes with subcell resolution, *J. Comput. Phys.* 83 (1989) 148–184.
- [21] J.S. Hesthaven, *Numerical Methods for Conservation Laws: From Analysis to Algorithms*, Comput. Sci. Eng., vol. 18, SIAM, Philadelphia, 2018.
- [22] E. Johnsen, On the treatment of contact discontinuities using WENO schemes, *J. Comput. Phys.* 230 (2011) 8665–8668.
- [23] S. Karni, A. Kurganov, Local error analysis for approximate solutions of hyperbolic conservation laws, *Adv. Comput. Math.* 22 (2005) 79–99.
- [24] S. Karni, A. Kurganov, G. Petrova, A smoothness indicator for adaptive algorithms for hyperbolic systems, *J. Comput. Phys.* 178 (2002) 323–341.
- [25] A. Kurganov, C.-T. Lin, On the reduction of numerical dissipation in central-upwind schemes, *Commun. Comput. Phys.* 2 (2007) 141–163.
- [26] A. Kurganov, Y. Liu, New adaptive artificial viscosity method for hyperbolic systems of conservation laws, *J. Comput. Phys.* 231 (2012) 8114–8132.
- [27] A. Kurganov, S. Noelle, G. Petrova, Semidiscrete central-upwind schemes for hyperbolic conservation laws and Hamilton-Jacobi equations, *SIAM J. Sci. Comput.* 23 (2001) 707–740.
- [28] A. Kurganov, E. Tadmor, Solution of two-dimensional Riemann problems for gas dynamics without Riemann problem solvers, *Numer. Methods Partial Differ. Equ.* 18 (2002) 584–608.
- [29] A. Kurganov, R. Xin, New low-dissipation central-upwind schemes, *J. Sci. Comput.* 96 (2023) 56.
- [30] P.D. Lax, Weak solutions of nonlinear hyperbolic equations and their numerical computation, *Commun. Pure Appl. Math.* 7 (1954) 159–193.
- [31] R.J. LeVeque, *Finite Volume Methods for Hyperbolic Problems*, Cambridge Texts in Appl. Math., Cambridge University Press, Cambridge, UK, 2002.
- [32] K.-A. Lie, S. Noelle, On the artificial compression method for second-order nonoscillatory central difference schemes for systems of conservation laws, *SIAM J. Sci. Comput.* 24 (2003) 1157–1174.
- [33] R. Liska, B. Wendroff, Comparison of several difference schemes on 1D and 2D test problems for the Euler equations, *SIAM J. Sci. Comput.* 25 (2003) 995–1017.
- [34] R. Löhner, An adaptive finite element scheme for transient problems in CFD, *Comput. Methods Appl. Mech. Eng.* 61 (1987) 323–338.
- [35] I. Menshov, P. Pavlukhin, On defragmentation algorithms for gpu-native octree-based amr grids, in: *Parallel Computing Technologies*, Springer, Cham, 2021, pp. 235–244.
- [36] H. Nessyahu, E. Tadmor, Nonoscillatory central differencing for hyperbolic conservation laws, *J. Comput. Phys.* 87 (1990) 408–463.
- [37] G. Puppo, M. Semplice, Numerical entropy and adaptivity for finite volume schemes, *Commun. Comput. Phys.* 10 (2011) 1132–1160.
- [38] J. Qiu, C.-W. Shu, On the construction, comparison, and local characteristic decomposition for high-order central WENO schemes, *J. Comput. Phys.* 183 (2002) 187–209.

- [39] J. Qiu, C.-W. Shu, A comparison of troubled-cell indicators for Runge-Kutta discontinuous Galerkin methods using weighted essentially nonoscillatory limiters, SIAM J. Sci. Comput. 27 (2005) 995–1013.
- [40] C.W. Schulz-Rinne, Classification of the Riemann problem for two-dimensional gas dynamics, SIAM J. Math. Anal. 24 (1993) 76–88.
- [41] C.W. Schulz-Rinne, J.P. Collins, H.M. Glaz, Numerical solution of the Riemann problem for two-dimensional gas dynamics, SIAM J. Sci. Comput. 14 (1993) 1394–1414.
- [42] J. Shi, Y.-T. Zhang, C.-W. Shu, Resolution of high order WENO schemes for complicated flow structures, J. Comput. Phys. 186 (2003) 690–696.
- [43] C.-W. Shu, Essentially non-oscillatory and weighted essentially non-oscillatory schemes, Acta Numer. 5 (2020) 701–762.
- [44] C.-W. Shu, S. Osher, Efficient implementation of essentially non-oscillatory shock-capturing schemes, J. Comput. Phys. 77 (1988) 439–471.
- [45] C.-W. Shu, S. Osher, Efficient implementation of essentially nonoscillatory shock-capturing schemes. II, J. Comput. Phys. 83 (1989) 32–78.
- [46] P.K. Sweby, High resolution schemes using flux limiters for hyperbolic conservation laws, SIAM J. Numer. Anal. 21 (1984) 995–1011.
- [47] E.F. Toro, Riemann Solvers and Numerical Methods for Fluid Dynamics: A Practical Introduction, third ed., Springer-Verlag, Berlin, Heidelberg, 2009.
- [48] M.J. Vuik, J.K. Ryan, Automated parameters for troubled-cell indicators using outlier detection, SIAM J. Sci. Comput. 38 (2016) A84–A104.
- [49] H. Wakimura, S. Takagi, F. Xiao, Symmetry-preserving enforcement of low-dissipation method based on boundary variation diminishing principle, Comput. Fluids 233 (2022) 105227.
- [50] B.S. Wang, W.S. Don, Z. Gao, Y.H. Wang, X. Wen, Hybrid compact-WENO finite difference scheme with radial basis function based shock detection method for hyperbolic conservation laws, SIAM J. Sci. Comput. 40 (2018) A3699–A3714.
- [51] B.S. Wang, W.S. Don, N.K. Garg, A. Kurganov, Fifth-order A-WENO finite-difference schemes based on a new adaptive diffusion central numerical flux, SIAM J. Sci. Comput. 42 (2020) A3932–A3956.
- [52] B.-S. Wang, P. Li, Z. Gao, W.S. Don, An improved fifth order alternative WENO-Z finite difference scheme for hyperbolic conservation laws, J. Comput. Phys. 374 (2018) 469–477.
- [53] W. Wang, C.-W. Shu, H.C. Yee, D.V. Kotov, B. Sjögreen, High order finite difference methods with subcell resolution for stiff multispecies discontinuity capturing, Commun. Comput. Phys. 17 (2015) 317–336.
- [54] X. Wen, W.S. Don, Z. Gao, J.S. Hesthaven, An edge detector based on artificial neural network with application to hybrid compact-WENO finite difference scheme, J. Sci. Comput. 83 (2020) 49.
- [55] P. Woodward, P. Colella, The numerical solution of two-dimensional fluid flow with strong shocks, J. Comput. Phys. 54 (1988) 115–173.
- [56] Y. Zheng, Systems of Conservation Laws. Two-Dimensional Riemann Problems, Progress in Nonlinear Differential Equations and Their Applications, Birkhäuser Boston, Inc., Boston, MA, 2001.